Chemistry–A European Journal
Research Article
doi.org/10.1002/chem.202400651
Chemistry Europe
European Chemical Societies Publishing
www.chemeurj.org

Hot Paper

Grain Boundary Defect Engineering in Rutile Iridium Oxide Boosts Efficient and Stable Acidic Water Oxidation

Ning Zhang[+],[a, b] Yingqi Fan[+],[a, b] Depeng Wang,[a, b] Hong Yang,[a, b] Yang Yu,[a] Jianwei Liu,[a, b] Jianrong Zeng,[c, d] Di Bao,*[a] Haixia Zhong,*[a, b] and Xinbo Zhang*[a, b]

Proton exchange membrane water electrolysis (PEMWE) is considered a promising technology for coupling with renewable energy sources to achieve clean hydrogen production. However, constrained by the sluggish kinetics of the anodic oxygen evolution reaction (OER) and the acidic abominable environment render the grand challenges in developing the active and stable OER electrocatalyst, leading to low efficiency of PEMWE. Herein, we develop the rutile-type IrO_2 nanoparticles with abundant grain boundaries and the continuous nanostructure through the joule heating and sacrificial template method. The optimal candidate (350-IrO_2) demonstrates remarkable electrocatalytic activity and stability during the OER, presenting a promising advancement for efficient PEMWE. DFT calculations verified that grain boundaries can modulate the electronic structure of Ir sites and optimize the adsorption of oxygen intermediates, resulting in the accelerated kinetics. 350-IrO_2 affords a rapid OER process with 20 times higher mass activity (0.61 A mg_{Ir}^{-1}) than the commercial IrO_2 at 1.50 V vs. RHE. Benefiting from the reduced overpotential and the preservation of the stable rutile structure, 350-IrO_2 exhibits the stability of 200 h test at 10 mA cm^{-2} with only trace decay of 11.8 mV. Moreover, the assembled PEMWE with anode 350-IrO_2 catalyst outputs the current density up to 2 A cm^{-2} with only 1.84 V applied voltage, long-term operation for 100 h without obvious performance degradation at 1 A cm^{-2}.

1. Introduction

Hydrogen is a vital carrier for efficiently utilizing renewable energy.[1] Proton exchange membrane water electrolysis (PEMWE) in acidic media offers advantages including high current density, fast system response, and low resistance losses for large-scale hydrogen generation.[2] However, the sluggish four-electron transfer process for oxygen evolution reaction (OER) leads to high catalytic overpotentials, severely limiting the efficiency of water electrolysis.[3] The previous works have made significant progress in enhancing the OER performance via using Ir-based electrocatalysts, however, it is still difficult to realize the underlying improvement in activity.[4] Moreover, their poor stability in acidic environments and high oxidation potentials severely limit the practical PEMWE application.[5] The serious issues of low mass activity and durability persist in current industrial Ir-based catalysts, for which it is urgent to develop OER electrocatalysts with high catalytic activity and stability.

IrO_2 with thermodynamically suitable interaction with oxygen intermediates, is regarded as the promising OER electrocatalyst.[6] Attributed to the strong connectivity between [IrO_6] cells in the rutile structure, rutile IrO_2 has the lower metal cation leaching rate and higher stability in acidic media.[7] Therefore, numerous efforts are dedicated to improve the activity of rutile IrO_2 while maintaining its superiority in durability. For metal oxides, optimizing the surface electronic structure and the absorption of intermediates through the well-designed strategies is explored to improve the catalytic performance, such as foreign atoms doping,[8] defects engineering,[9] etc. Doping with foreign metal atoms, such as Ce,[10] Re,[11] and Ta[12] in rutile IrO_2 has been effective in enhancing activity for the Ir active sites. In addition, constructing defects related to both anionic[13] (O^{2-}) and cationic[14] (Ir^{4+} or foreign atoms) species, will alter the covalency of Ir–O bonds and thereby affect the adsorption free energy of *OH and *O intermediates. Grain boundaries (GBs) are a special type of defect, which can be introduced into crystalline materials through kink nucleation and propagation.[15] The irregular arrangement of the atoms near GBs can significantly impact the intrinsic properties of the materials and enhance the OER activity. Inspired by the above facts, IrO_2 electrocatalysts with stable rutile structure and rich GBs defects may potentially possess high mass activity and stability for acidic OER and

[a] N. Zhang,[+] Y. Fan,[+] D. Wang, H. Yang, Y. Yu, J. Liu, D. Bao, H. Zhong, X. Zhang
State Key Laboratory of Rare Earth Resource Utilization
Changchun Institute of Applied Chemistry
Chinese Academy of Sciences
Changchun 130022, China
E-mail: dbao@ciac.ac.cn
hxzhong@ciac.ac.cn
xbzhang@ciac.ac.cn

[b] N. Zhang,[+] Y. Fan,[+] D. Wang, H. Yang, J. Liu, H. Zhong, X. Zhang
School of Applied Chemistry and Engineering
University of Science and Technology of China
Hefei 230026, China

[c] J. Zeng
Shanghai Synchrotron Radiation Facility, Shanghai Advanced Research Institute, Chinese Academy of Sciences, Shanghai 201204, China

[d] J. Zeng
Shanghai Institute of Applied Physics, Chinese Academy of Sciences, Shanghai 201800, China

[+] These two authors contribute equally to this work.

Supporting information for this article is available on the WWW under https://doi.org/10.1002/chem.202400651

enhance the overall efficiency of PEMWE. However, the controlled synthesis of this IrO_2, and well understanding of the GBs in boosting the acidic OER remain challenges.

Herein, we develop the rutile IrO_2 electrocatalysts with interconnected nanostructure and abundant GBs by using rapid joule heating pyrolysis and sacrificial template strategy. The target 350-IrO_2 exhibits a high acidic OER activity with a low overpotential of 246 mV at 10 mA cm^{-2}, which is significantly more active than IrO_2 without GBs (477 mV) and commercial IrO_2 (377 mV). Density function theory (DFT) calculations reveal that the electronic structure of Ir and the covalency of Ir–O are adjusted by engineering rich GBs, and the enhanced activity is attributed to the reduced energy barriers for the adsorption intermediates on these optimized Ir sites. Benefiting from the advantage of stable rutile structure, 350-IrO_2 also presents high stability without the obvious potential degradation under 200 h continuous operation at 10 mA cm^{-2}. Importantly, the assembled PEMWE device with the anode 350-GBs–IrO_2 catalyst achieves a current density of 2 A cm^{-2} at 1.84 V voltage and demonstrates the potential for practical application.

2. Results and Discussion

2.1. Synthesis and Characterization

The synthesis process of rutile IrO_2 with rich GBs is illustrated in Figure 1a and can be summarized in four steps of electrospinning, wetness impregnation, joule heating, and calcination. First, a modified electrospinning method[16] (details in Experimental 2.2) was employed to prepare the high surface area porous carbon nanofibers (PCNFs), which are used as the substrate for the subsequent synthesis. The field-emission scanning electron microscope (SEM, Figure S1) shows the fiber morphology of PCNF. And transmission electron microscope (TEM, Figure S2) image reveals that PCNFs with a uniform diameter of approximately 500 nm were successfully prepared. $IrCl_3$ was distributed on the surface of PCNFs through a simple wetness impregnation process. Subsequently, a programmable temperature-controlled joule heating method was used for the pyrolysis of $IrCl_3$ in which the high temperature and appropriate insulation time can ensure the complete decomposition of $IrCl_3$. Notably, the ultrafast pyrolysis process via joule heating with the temperature up to 1750 °C within 0.1 seconds and rapid cooling (Figure S3) in the Ar atmosphere is conducive to the generation of the extremely small metallic Ir nanoparticles.[17] The SEM of Ir-PCNF (Figure S1b) indicated the maintenance of PCNFs during joule heating. Combined with TEM images and the X-ray diffraction (XRD) results in Figures S4a and S5, ultrasmall nanoparticles uniformly loaded onto PCNFs with a diameter of approximately 1.6 nm and clear lattice fingers are assigned to the metallic Ir. The XPS spectra of Ir-PCNF show a lower binding energy compared to commercial IrO_2 (C–IrO_2) in Figure S6a, further confirming the metallic state of Ir. The possible Cl^- preservation of Ir-PCNFs was not detected according to the Cl 2p X-ray photoelectron spectroscopy (XPS, Figure S6b) results, which confirms the complete transformation of $IrCl_3$ into Ir nanoparticles.

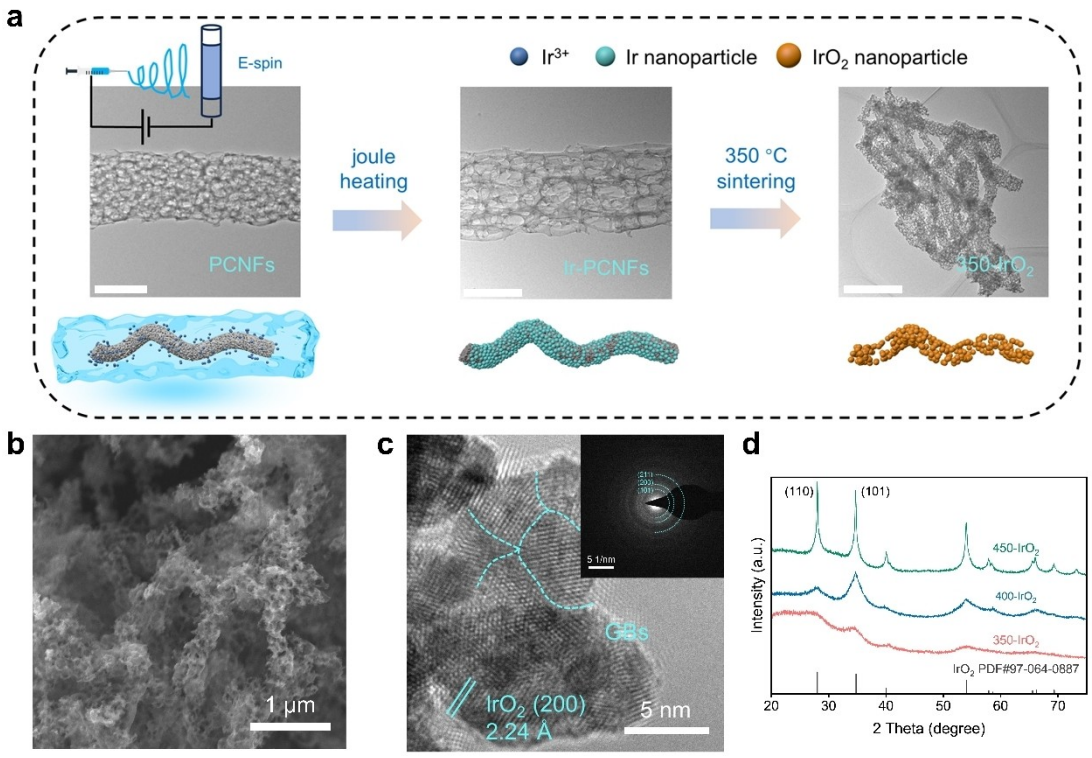

Figure 1. (a) The schematic routes for synthesizing 350-IrO_2. (scar bar, 200 nm) (b) SEM image of 350-IrO_2. (c) HR-TEM image of 350-IrO_2 (inset graph is SAED image of 350-IrO_2). (d) The XRD patterns of 350-IrO_2, 400-IrO_2, and 450-IrO_2.

IrO_2 is obtained from Ir-PCNFs after calcination at different temperatures in air and the 350-IrO_2 is prepared at 350 °C. The lower temperature as 300 °C is not sufficient to drive the conversion of elemental Ir into IrO_2 and the oxidative removal of PCNF, so the precursors (Ir-PCNF) is unchanged after calcination at 300 °C (TEM image, Figure S7). 350-IrO_2 sample also inherited the fiber morphology of PCNF template except with rough surface (SEM image, Figure 1b). The high-resolution resolution-transmission electron microscope (HR-TEM) image of 350-IrO_2 (Figure 1c) reveals that the metallic Ir was oxidized into rutile IrO_2 nanoparticles with a slightly increased particle size, along with generating abundant grain boundaries (GBs) during the crystal propagation process. Distinct polycrystalline diffraction rings attributed to IrO_2 nanoparticles are observed in the selected area electron diffraction (SAED, Figure 1c inset) diagram of 350-IrO_2. The uniform distribution of Ir and O elements in energy-dispersive X-ray spectroscopy (EDX, Figure S8) further indicates the oxidation of Ir nanoparticles into IrO_2 at 350 °C. As shown in the TEM profiles (Figure S9) and XRD patterns (Figure 1d), when the sintering temperature is increased (400 and 450 °C), the resultant 400-IrO_2, and 450-IrO_2 exhibit similar oxidation and propagation processes with 350-IrO_2. Among them, the size of IrO_2 nanoparticles significantly increases upon the increase in sintering temperature, which might lead to a reduction in GBs content. Interestingly, the (110) crystal plane of rod-shaped rutile-phase iridium dioxide was observed in 450-IrO_2, whereas this specific orientation was absent in 350-IrO_2 or 400-IrO_2, which is consistent with the XRD results. The broadening of full width at half maximum (FWHM) of prepared electrocatalyst in XRD patterns further verified the size growth of the IrO_2 nanoparticles with the increase in calcination temperature, in accordance with the TEM results. Moreover, the increased intensity of the (110) diffraction peak indicates the beneficial growth of the thermodynamically stable (110) crystal face in 450-IrO_2. However, this oriented growth is not observed in 350-IrO_2 and 400-IrO_2. It is thus clear that the GBs between crystal faces in these synthesized IrO_2 will be enriched upon decreasing the pyrolysis temperature, which likely facilitates the OER process on IrO_2.

The electronic configuration and local coordination information of prepared electrocatalysts were collected by XPS and synchrotron X-ray absorption spectroscopy (XAS) spectra. As displayed in Figure 2a, the high-resolution O 1s XPS spectra can be deconvoluted into three peaks: the oxygen in adsorbed water (O_{H2O}) at 529.8 eV, the lattice oxygen (O_{lat}) at 526.0 eV and the adsorbed oxygen (O_{ad}) at 528.0 eV. The result indicates (Table S1) the lowest surface O_{lat} content (12.42 %) in 350-IrO_2, which is likely attributed to the unsaturated coordination Ir sites formed by the abundant GBs defects. The white line peak intensity in X-ray absorption near edge structure (XANES, Figure 2b) spectrum at Ir L_3-edge is proportional to the oxidation state of Ir, indicating the reduction in valence state caused by unsaturated coordination sites.[18] As shown in Ir 4f XPS spectra (Figure 2c), the lower binding energy of 350-IrO_2 further verified the lower Ir valence state compared to the controlled samples and C–IrO_2. Furthermore, the analyses of the

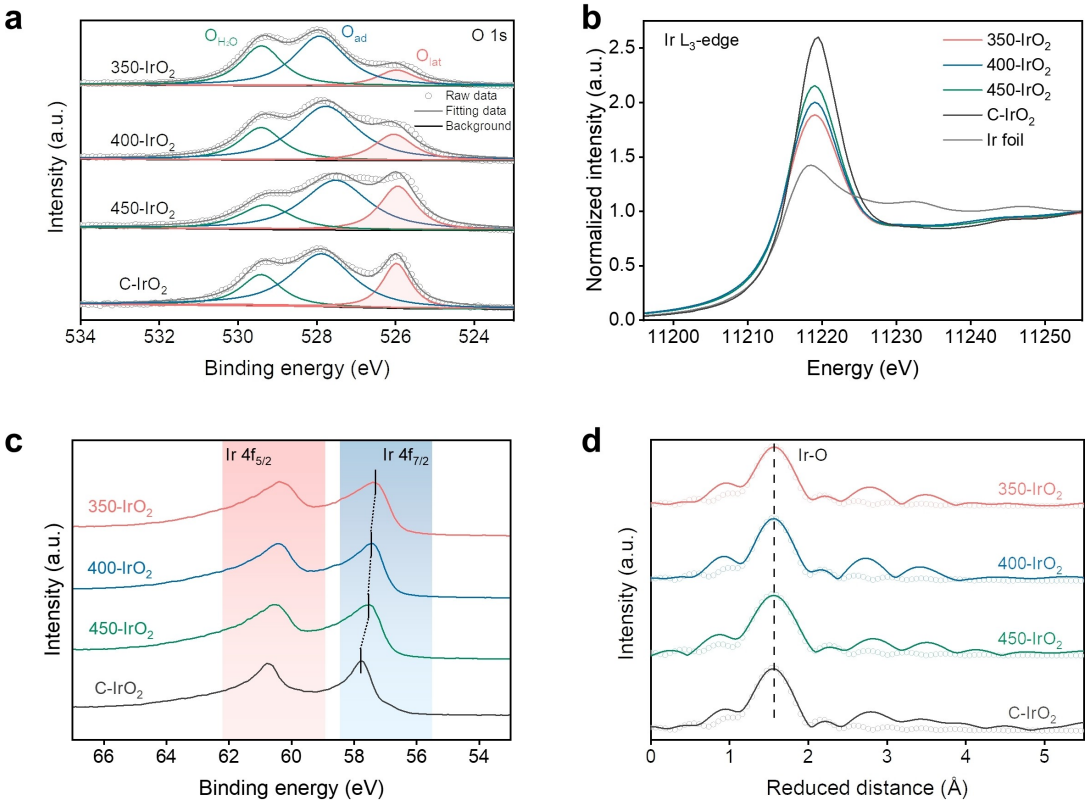

Figure 2. (a) O 1s XPS spectra of 350-IrO_2, 400-IrO_2, and 450-IrO_2. (b) Ir L_3-edge XANES spectra of 350-IrO_2, 400-IrO_2, 450-IrO_2, Ir foil, and C–IrO_2. (c) Ir 4f XPS spectra of 350-IrO_2, 400-IrO_2, 450-IrO_2, and C–IrO_2 (d) EXAFS spectra of 350-IrO_2, 400-IrO_2, 450-IrO_2, and C–IrO_2.

extended X-ray absorption fine structure (EXAFS, Figure 2d) spectra are conducted. The corresponding fitting results of the first shell Ir–O (Figure S10 and Table S2) reveal the coordination structures of 350-IrO_2, 400-IrO_2, 450-IrO_2, and C–IrO_2. The series electrocatalysts of IrO_2 with GBs exhibit nearly similar Ir–O bond lengths compared to the commercial rutile IrO_2 (C–IrO_2), indicating the preservation of the stable rutile structure, which is comprised of the Ir atom as the coordination center and the [IrO_6] octahedra serves as the basic hexacoordinated structural units.[19] Differently, the coordination number (CN) of Ir for 350-IrO_2, 400-IrO_2, and 450-IrO_2 decreases along with reducing the sintering temperature. The decrease in the CN value is ascribed to a large population of surface and corner Ir atoms arising from the GBs,[20] which agrees well with the morphology and XPS analysis.

The control samples (350-no GBs and 450-no JH (JH: joule heating) are also prepared to evaluate the influence of GBs and joule heating pretreatment, respectively. It is worth noting that the PCNF as a sacrificed template is important for generating IrO_2. For comparison, carbon nanotubes (CNTs) are chosen as the template due to their feature of higher graphitization, providing enhanced oxidation resistance in air. Similarly, after wet impregnating and joule heating to load Ir nanoparticles, the 350-no GBs is obtained after calcination at 350 °C. TEM and XRD (Figure S11) analysis confirms the successful synthesis of IrO_2 nanoparticles with approximately 2 nm in diameter independently distributed on the surface of CNTs. Differently, GBs were not observed in 350-no GBs. In addition, the counterpart (450-no JH) synthesized by the traditional heating process rather than the joule heating was also synthesized. A minimum pyrolysis temperature of 450 °C is required for the complete conversion of iridium salts into IrO_2 during the slow heating process because of the fact that the decomposition and oxidation temperature of $IrCl_3$ is higher than the direct oxidation temperature of metallic Ir nanoparticles. Compared to 450-IrO_2, the uneven distribution of IrO_2 nanoparticles is observed in 450-no JH as indicated by the TEM results (Figure S12). Thus, the rapid pyrolysis via the joule heating pretreatment is effective in reducing the phase transition temperature of iridium salts into the IrO_2, resulting in finer nanoparticles and facilitating the enrichment of GBs.

2.2. Electrochemical Acidic OER Analysis

The electrocatalytic OER activities of the synthesized samples were evaluated in 0.5 M H_2SO_4 with a three-electrode system. As shown in the OER polarization curves in Figure 3a, 350-IrO_2 only requires a lower overpotential of 246 mV than that of commercial IrO_2 (C–IrO_2) with 376 mV to achieve the benchmark current density of 10 mA cm^{-2}. Along with the reduced pyrolysis temperature (450–350 °C), overpotential at 10 mA cm^{-2} for these samples under various pyrolysis temperatures is decreased with the order of 350-IrO_2 (246 mV) < 400-IrO_2 (260 mV) < 450-IrO_2

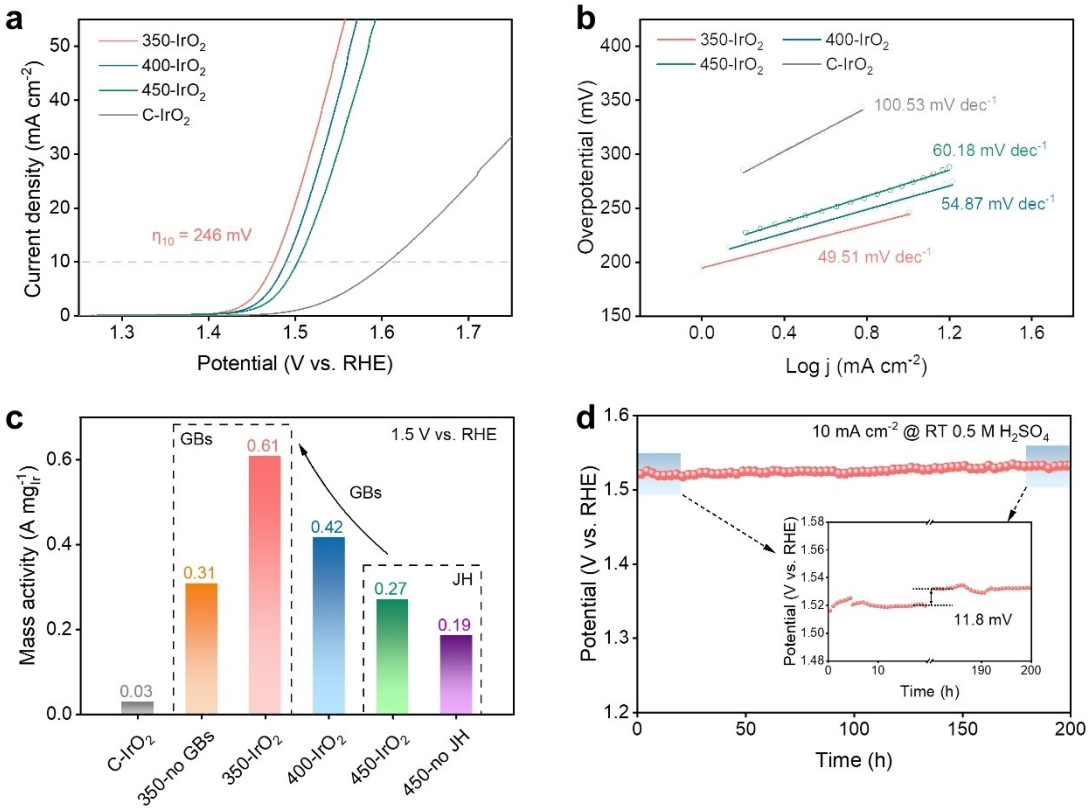

Figure 3. (a) Geometric area normalized LSV curves of 350-IrO_2, 400-IrO_2, 450-IrO_2, and C–IrO_2. (b) Tafel plots of 350-IrO_2, 400-IrO_2, 450-IrO_2 and C–IrO_2. (c) Mass activities normalized by the Ir mass of the various electrocatalysts at 270 mV (1.5 V vs. RHE). (d) CP curve and magnified inset of 350-IrO_2. RT: room temperature.

(273 mV), which are all lower than 350-no GBs (477 mV) and 450-no JH (287 mV) as shown in Figure S14. These results verify a positive correlation between the content of GBs defects and OER activity. Moreover, 350-IrO_2 exhibits a lower Tafel slope (Figure 3b and S15) of 49.51 mV dec^{-1}, compared to the 400-IrO_2 (54.87 mV dec^{-1}), 450-IrO_2 (60.18 mV dec^{-1}), and C–IrO_2 (100.53 mV dec^{-1}), which indicated the fast reaction kinetics on the active surface. Additionally, the mass activity normalized by the Ir mass at 1.5 V vs. RHE (overpotential = 270 mV) is shown in Figure 3c and S14. The activity superiority of 350-IrO_2 is further gleaned from its highest mass activity as 0.61 A mg_{Ir}^{-1} compared to the counterparts. After excluding the influence of factors such as particle size and synthesis temperature, 350-no GBs shows obviously lower mass activity (0.31 A mg_{Ir}^{-1}), which strongly indicates that GBs significantly enhance the OER activity. The double-layer capacitance (C_{dl}, Figure S16) of all the electrocatalysts is estimated by voltammetry (CV) curves measured at different scan rates in non-faraday potential regions to evaluate their electrochemically active surface areas (ECSA).[21] The 350-IrO_2 shows the highest C_{dl} value as 162.2 mF cm^{-2}, suggesting its higher ECSA with exposure to more accessible active sites. The better acidic OER activity of 350-IrO_2 is further confirmed by the electrochemical impedance spectroscopy (EIS) measurements in Figure S17. The charge transfer resistance (R_{ct}) of 350-IrO_2 is as low as 10 Ω, indicating the fast charge transfer on the surface, which can contribute to the fast reaction kinetics.

To evaluate the stability of the 350-IrO_2 under the corrosive acidic and oxidation conditions, chronopotentiometry (CP) is carried out in 0.5 M H_2SO_4. As shown in Figure 3d, only a trace potential increase of 11.8 mV for 350-IrO_2 is observed after the continuous OER operation for 200 h. However, the activity of C–IrO_2 experienced terrible decay after operating for 1.5 h CP test (Figure S18), indicating better acidic OER durability for 350-IrO_2. In addition, 350-IrO_2 exhibits high activity and stability conpared twith other advanced Ir based catalysts in Table S3. The S-number, which is defined as the ratio of the amount of generated oxygen and the dissolved iridium into the electrolyte, was further utilized to illustrate the stability of the catalyst.[13] According to the inductively coupled plasma-mass spectroscopy (ICP-MS, Table S3), it is calculated to be 2.50×10^4 for 350-IrO_2, revealing its good acidic corrosion and stability during OER process. Furthermore, TEM (Figure S19a) results after the OER test of 350-IrO_2 show no significant changes in structure and morphology, highlighting the good stability of 350-IrO_2. Similarly, 350-IrO_2 maintains the rutile structure after the long-term OER tests as indicated by the XRD pattern (Figure S19b) results.

Encouraged by the high activity and stability of acidic OER in a three-electrode configuration, a catalyst-coated membrane (CCM) using 350-IrO_2 as anode is employed to evaluate its performance in a PEMWE device. The polarization curve (Figure 4a) operated at 80 °C exhibits high activity of the output voltage of 1.68 V and 1.84 V at 1 A cm^{-2} and 2 A cm^{-2}, respectively. The long-term stability (Figure 4b) could be operated at 1 A cm^{-2} for at least 100 h without obvious performance decay. And the S-number (Table S4) of 350-IrO_2 is 5.33×10^7 in the PEMWE configuration. The high performance of 350-IrO_2 in PEMWE highlights the feasibility of 350-IrO_2 in practical application.

2.3. DFT Calculations

Density functional theory (DFT) calculations are conducted to further understand the origin of the OER activity of 350-IrO_2 with rich GBs as compared to rutile IrO_2. The thermodynamically stable (110) facet is chosen to model the rutile IrO_2[22] (Figure S20a). Given the complexity of crystal facets of the synthesized IrO_2, the predominant (110) and (101) facets are selected for 350-IrO_2 (Figure S20b).

Based on the computed projected density of state (PDOS, Figure 5a and 5b) results, the electrons near the Fermi level become delocalized in rutile IrO_2 with GBs compared to rutile IrO_2, indicating the role of GBs engineering in tuning the electronic structure of IrO_2. The proximity of the Ir 5d–band center (ε_d) to the Fermi level in the GBs model (−2.165 eV) demonstrates the enhanced binding ability between Ir active sites and oxygen intermediates.[23] Additionally, with the Fermi level energy lowering the energy and moving closer to O 2p states in rutile IrO_2 with GBs ($\varepsilon_p = -3.37$ eV) compared to the rutile IrO_2 ($\varepsilon_p = -4.39$ eV), the covalency of the Ir–O bond is

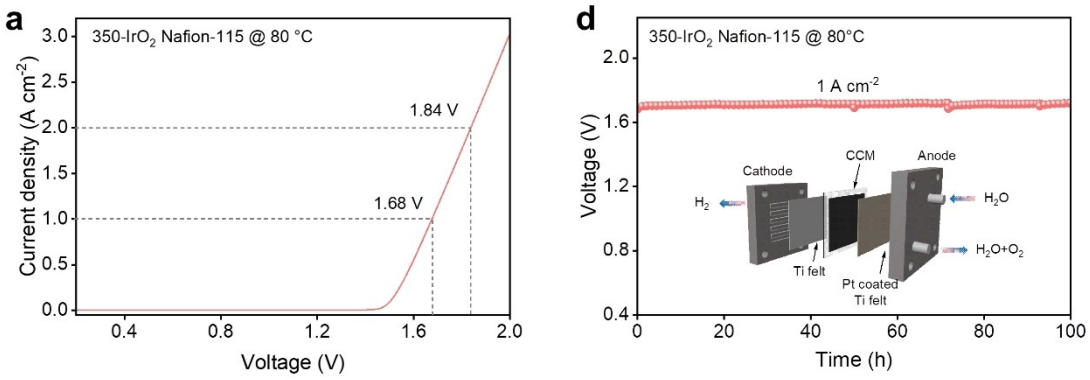

Figure 4. (a) Polarization curve of the PEMWE using 350-IrO_2 as anode electrocatalyst. (b) Chronopotentiometry curve of the PEMWE using 350-IrO_2 as anode electrocatalyst operated at 1 A cm^{-2} (inset shows the schematics of PEMWE).

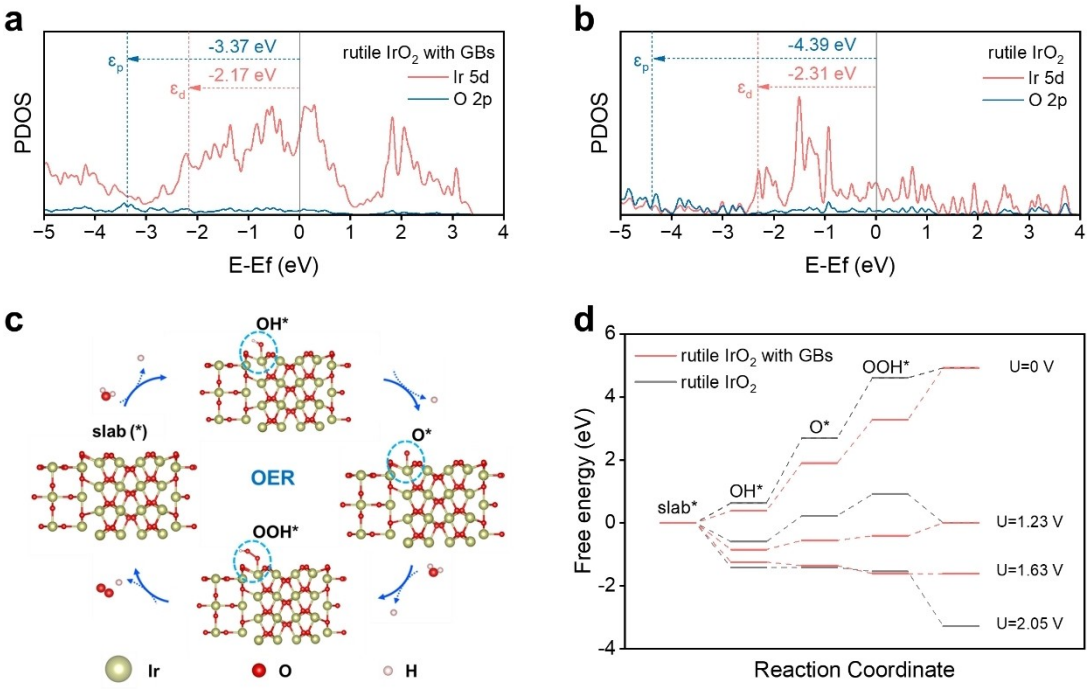

Figure 5. (a–b) Computed DOS of rutile IrO_2 with GBs and rutile IrO_2. (c) The optimized structures of oxygen intermediates adsorption on IrO_2 with GBs. (d) Calculated free energy diagrams of IrO_2 with GBs and rutile IrO_2.

enhanced by the presence of GBs wherein strong covalency of Ir–O is associated with the high OER activity. Therefore, when the O 2p states approach the Fermi level, water decomposition becomes more thermodynamically favorable.[24] It is thus clear that GBs can modulate the electronic structure of surface Ir active sites, thereby influencing the adsorption behavior of oxygen intermediates and enhancing OER activity through an increase in covalency.[25]

The adsorbate evolution mechanism (AEM) is widely accepted for the crystallized IrO_2 and it was confirmed with numerous experimental investigations.[26] In this mechanism, OER at applied electrocatalysts proceeds via four proton-coupled electron transfer (PCET) steps (Figure 5c and S21) with OH*, O*, and *OOH intermediates, respectively. Figure 5d illustrates the free energy diagrams calculated on both the surfaces of rutile IrO_2 with and without GBs. The second proton-couple electron transfer step (OH*→O*) with the highest energy uptake ($\Delta G_2 = 2.1$ eV, Table S5) is the potential determined step (PDS) on rutile IrO_2. The introduction of GBs significantly decreases ΔG_2 for 350-IrO_2 (1.5 eV) and thus changes the PDS to the last step (OOH*→slab*) with the energy barrier as 1.6 eV. Combining the PDOS results, it is evident that GBs optimize the adsorption capacity of Ir active sites for oxygen species, thereby lowering the reaction barrier. Thus, it requires only 1.63 V to drive the OER reaction for rutile IrO_2 with GBs. The free energy calculations suggest that GBs effectively contribute to optimizing the adsorption of oxygen intermediates at Ir sites toward fast OER kinetics.

3. Conclusions

In summary, we optimized the pathway from iridium chloride pyrolysis into IrO_2 by joule heating pretreatment, resulting in ultrasmall IrO_2 nanoparticles with abundant GBs and uniform particle size. The optimal 350-IrO_2 exhibits high activity and stability with a low overpotential of 246 mV and stability of 200 h at 10 mA cm^{-2}. DFT calculations reveal that GBs modify the surface electronic structures, thus leading to the appropriate adsorption ability on Ir sites and enhancing the OER activity. Benefiting from the controllable synthesis and the introduction of GB defects, the prepared 350-IrO_2 enables highly efficient and stable hydrogen production in PEMWE under 1 A cm^{-2}. This work not only presents one promising OER electrocatalyst for the efficient PEMWE but also provides ideas for engineering grain boundary defects in nanocatalysts and understanding the correlation between the surface structure and OER performance.

4. Supporting Information

Supporting Information is available from the Wiley Online Library or from the author.

Acknowledgements

This work was supported by the National Key R&D Program of China (2022YFB4002201), the National Natural Science Foundation of China (52273277, 52072362, 52171194), Jilin Province

Science and Technology Development Plan Funding Project (SKL202302039 and 20230201150GX) and Youth Innovation Promotion Association CAS (2021223). These authors thank the staff of beamline BL13SSW at Shanghai Synchrotron Radiation Facility for experiment support. H.-X. Zhong acknowledges funding from the National Natural Science Foundation of China Outstanding Youth Science Foundation of China (Overseas).

Conflict of Interests

The authors declare no conflict of interest.

Data Availability Statement

The data that support the findings of this study are available from the corresponding author upon reasonable request.

Keywords: water electrolysis · acidic oxygen evolution reaction · electrocatalysts · joule heating · rutile-type IrO_2 · grain boundary

[1] N. Du, C. Roy, R. Peach, M. Turnbull, S. Thiele, C. Bock, *Chem. Rev.* **2022**, *122*, 11830–11895.
[2] T. Terlouw, C. Bauer, R. McKenna, M. Mazzotti, *Energy Environ. Sci.* **2022**, *15*, 3583–3602.
[3] X. Xie, L. Du, L. Yan, S. Park, Y. Qiu, J. Sokolowski, W. Wang, Y. Shao, *Adv. Funct. Mater.* **2022**, *32*, 2110036.
[4] a) X. Qin, D. Kim, Y. Piao, *Carbon Energy* **2020**, *3*, 66–100; b) L. Tang, Y. Rao, L. Wei, H. Zheng, H. Liu, W. Zhang, K. Tang, *Chin. J. Chem.* **2021**, *39*, 2692–2698.
[5] a) C. Rong, K. Dastafkan, Y. Wang, C. Zhao, *Adv. Mater.* **2023**, *35*, 2211884; b) Y. Wang, M. Zhang, Z. Kang, L. Shi, Y. Shen, B. Tian, Y. Zou, H. Chen, X. Zou, *Nat. Commun.* **2023**, *14*, 5119.
[6] A. Loncar, D. Escalera-Lopez, S. Cherevko, N. Hodnik, *Angew. Chem. Int. Ed.* **2022**, *61*, e202114437.
[7] S. Cherevko, S. Geiger, O. Kasian, N. Kulyk, J.-P. Grote, A. Savan, B. R. Shrestha, S. Merzlikin, B. Breitbach, A. Ludwig, K. J. J. Mayrhofer, *Catal. Today* **2016**, *262*, 170–180.
[8] Y. Huang, M. Li, F. Pan, Z. Zhu, H. Sun, Y. Tang, G. Fu, *Carbon Energy* **2022**, *5*, e279.
[9] N. Yao, J. Zhu, H. Jia, H. Cong, W. Luo, *Chin. J. Chem.* **2023**, *42*, 343–350.
[10] Y. Wang, S. Hao, X. Liu, Q. Wang, Z. Su, L. Lei, X. Zhang, *ACS Appl. Mater. Interfaces* **2020**, *12*, 37006–37012.
[11] W. Huo, X. Zhou, Y. Jin, C. Xie, S. Yang, J. Qian, D. Cai, Y. Ge, Y. Qu, H. Nie, Z. Yang, *Small* **2023**, *19*, 2022207847.
[12] N. Zhang, J. Du, N. Zhou, D. Wang, D. Bao, H. Zhong, X. Zhang, *Chin. J. Catal.* **2023**, *53*, 134–142.
[13] H. N. Nong, T. Reier, H.-S. Oh, M. Gliech, P. Paciok, T. H. T. Vu, D. Teschner, M. Heggen, V. Petkov, R. Schlögl, T. Jones, P. Strasser, *Nat. Catal.* **2018**, *1*, 841–851.
[14] Q. Qin, H. Jang, Y. M. Wang, L. J. Zhang, Z. J. Li, M. G. Kim, S. G. Liu, X. E. Liu, J. Cho, *Adv. Energy Mater.* **2021**, *11*, 2003561.
[15] H. K. Park, H. Ahn, T. H. Lee, J. Y. Lee, M. G. Lee, S. A. Lee, J. W. Yang, S. J. Kim, S. H. Ahn, S. Y. Kim, C. H. Lee, E. S. Park, H. W. Jang, *Small Methods* **2020**, *5*, 202000755.
[16] R. Liu, L. Hou, G. Yue, H. Li, J. Zhang, J. Liu, B. Miao, N. Wang, J. Bai, Z. Cui, T. Liu, Y. Zhao, *Adv. Fiber Mater.* **2022**, *4*, 604–630.
[17] J. Ahn, S. Park, D. Oh, Y. Lim, J. S. Nam, J. Kim, W. Jung, I.-D. Kim, *ACS Nano* **2023**, *17*, 12188–12199.
[18] J. Shan, C. Ye, S. Chen, T. Sun, Y. Jiao, L. Liu, C. Zhu, L. Song, Y. Han, M. Jaroniec, Y. Zhu, Y. Zheng, S. Z. Qiao, *J. Am. Chem. Soc.* **2021**, *143*, 5201–5211.
[19] Z. Fan, Y. Ji, Q. Shao, S. Geng, W. Zhu, Y. Liu, F. Liao, Z. Hu, Y.-C. Chang, C.-W. Pao, Y. Li, Z. Kang, M. Shao, *Joule* **2021**, *5*, 3221–3234.
[20] S. Hao, H. Sheng, M. Liu, J. Huang, G. Zheng, F. Zhang, X. Liu, Z. Su, J. Hu, Y. Qian, L. Zhou, Y. He, B. Song, L. Lei, X. Zhang, S. Jin, *Nat. Nanotechnol.* **2021**, *16*, 1371–1377.
[21] C. C. McCrory, S. Jung, J. C. Peters, T. F. Jaramillo, *J. Am. Chem. Soc.* **2013**, *135*, 16977–16987.
[22] F. Zhao, B. Wen, W. Niu, Z. Chen, C. Yan, A. Selloni, C. G. Tully, X. Yang, B. E. Koel, *J. Am. Chem. Soc.* **2021**, *143*, 15616–15623.
[23] Z.-F. Huang, J. Song, Y. Du, S. Xi, S. Dou, J. M. V. Nsanzimana, C. Wang, Z. J. Xu, X. Wang, *Nat. Energy* **2019**, *4*, 329–338.
[24] X. Rong, J. Parolin, A. M. Kolpak, *ACS Catal.* **2016**, *6*, 1153–1158.
[25] A. Grimaud, O. Diaz-Morales, B. Han, W. T. Hong, Y. L. Lee, L. Giordano, K. A. Stoerzinger, M. T. M. Koper, Y. Shao-Horn, *Nat. Chem.* **2017**, *9*, 457–465.
[26] J. Gao, C. Q. Xu, S. F. Hung, W. Liu, W. Cai, Z. Zeng, C. Jia, H. M. Chen, H. Xiao, J. Li, Y. Huang, B. Liu, *J. Am. Chem. Soc.* **2019**, *141*, 3014–3023.

Manuscript received: March 11, 2024
Accepted manuscript online: May 5, 2024
Version of record online: June 21, 2024